A Laser Doppler Blood Flow Measurement System With a 151.4 dBΩ Gain and 0.05% Nonlinearity for PAD Patients

Muhammad Asfandyar Awan, *Graduate Student Member, IEEE*, Moaaz Ahmed, *Member, IEEE*, and Bo Wang, *Member, IEEE*

***Abstract*—This article presents a compact blood flow measurement system exploiting the Doppler effect and photocurrent sensing technique for wearable health monitoring. Specifically, it helps the patients suffering from peripheral artery disease (PAD) to monitor the blood flow continuously without involving a physician or medical expert. The system prototype integrates a laser diode, a photodiode, and an analog front-end (AFE) on a 54 mm × 64 mm three-layer PCB using discrete components for proof of concept. The front-end is designed with two output modes providing simultaneous current-to-voltage and current-to-frequency conversion without requiring an external clock source. Moreover, this system does not require optical filters or fibers, dynamic artifacts are therefore significantly reduced. Drawing 33 mA current from a 3.3-V supply, the developed system offers a transimpedance gain of 151.4 dBΩ for the voltage mode output. For the frequency output, a nonlinearity of 0.05% is achieved.**

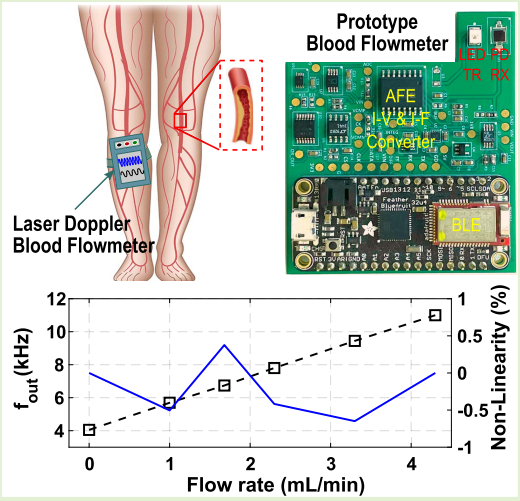

***Index Terms*— Blood flowmetry, current sensing, peripheral artery disease (PAD), Doppler effect, wearable sensors.**

I. Introduction

SMOOTH blood flow in the human body is vital to health as it supplies oxygen and nutrients to other organs. Any functional deficiencies in the heart and/or blood vessels will appear as a varied blood flow speed [1]. Several health issues, such as peripheral arterial disease (PAD), heart disease, body stiffness, numbness, and cerebrovascular disease may develop due to the obstruction of blood flow [2]. Specifically, PAD is a common blood circulatory problem in which narrowed arteries reduce blood flow to limbs [3]. It may lead to pain and several other symptoms like foot wounds, eventually leading to foot or leg amputation in severe cases. Individuals with PAD also have a much higher risk of heart attack or stroke. However, PAD sometimes has similar symptoms as other diseases which commonly occur around the same age. Therefore, it is essential to distinguish these underlying conditions for early and correct treatment.

Doppler ultrasound is a non-invasive and widely used method to estimate volumetric blood flow. However, it measures blood flow intermittently, resulting in errors caused by the angle of approach and operator variability [4]. Ankle-brachial pressure index is also often used to assess blood flow for PAD diagnosis [5]. However, some PAD patients with non-compressible lower extremity arteries may have falsely high ABIs, leading to wrong diagnosis and mistreatment [6]. Magnetic resonance imaging has also been applied to measure blood flow, but it is quite complex and costly to perform [7]. Laser Doppler flowmeters (LDFs), which use optical fibers as a spatial filter to conduct laser to skin tissues and send the collected reflected signal to a photodetector, can achieve a high signal-to-noise ratio [4]. It typically requires optical lenses, filters, and fibers with an aligned focal axis of each component. Although the optical probe is small, the movement of the optical fiber still affects its measurement. Currently, it is possible to measure blood flow with a hot wire convective

Manuscript received 4 May 2022; accepted 31 May 2022. Date of publication 13 June 2022; date of current version 14 July 2022. This work was supported by the Hamad Bin Khalifa University (HBKU) Innovation Grant under HBKU-INT-IC-IIF-05-01. The associate editor coordinating the review of this article and approving it for publication was Dr. Hui Jiang. *(Corresponding author: Bo Wang.)*

The authors are with the Division of Information and Computing Technology, College of Science and Engineering, Hamad Bin Khalifa University, Doha, Qatar (e-mail: bwang@hbku.edu.qa).

Digital Object Identifier 10.1109/JSEN.2022.3180927

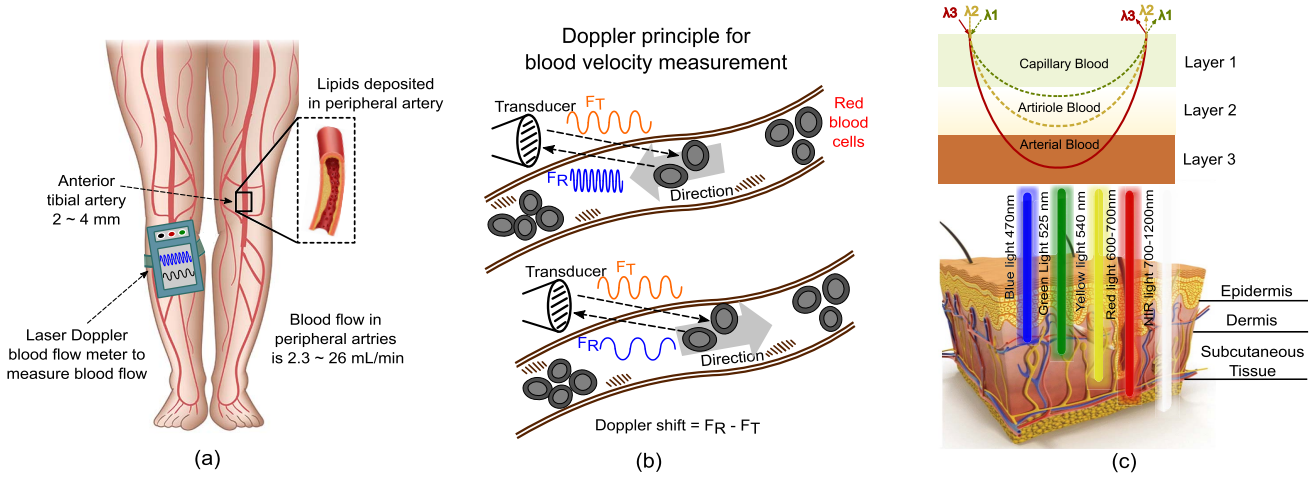

Fig. 1. (a) Illustration of a wearable laser Doppler blood flowmeter applied for peripheral arteries; (b) the principle of using Doppler effect to estimate blood velocity; (c) model of light and tissues interaction with three different wavelengths and how different lights penetrate the skin [21].

heating device, however, such device only measures a long-term averaged instead of instantaneous blood flow [7].

Several challenges are associated with these conventional blood flow measurement techniques. Particularly, they are often used in hospitals under the supervision of physicians and require other necessary facilities. Over the last decade, numerous homecare sensors and devices have been applied to monitor essential health conditions continuously and non-invasively [8]–[11]. Monitoring vital health signs such as blood flow with wearable sensors is becoming increasingly popular with time and will be "the next normal" in a near future.

In this paper, a miniaturized blood flowmeter prototype utilizing the laser Doppler effect is developed for PAD patients as illustrated in Fig. 1(a). Our proposed current readout in this prototype has a self-reset mechanism without requiring external clock. Hence, the system bandwidth is not limited by the speed of a master system clock. Another innovation of this readout is it employs only one integrator to achieve both current-to-frequency and current-to-voltage conversion, effectively reducing the device size and power consumption. This device operates in a voltage mode for small and fast input current signals, starting from 41.7 pA up to 80 nA in a bandwidth of 18.9 kHz. It can also switch to a frequency mode for input currents with larger magnitudes up to 650 nA. The designed readout achieves a measured nonlinearity error of 0.05%, and a transimpedance gain of 151.4 dBΩ for the current from the photodiode. Our designed flowmeter does not require an optical lens, spatial filters, and optical fibers to transmit and receive optical signals, thereby reducing noise and dynamic artifacts in addition to significant power, area, and cost savings compared to the existing LDFs [12]–[14].

This paper is organized as follows. Section II introduces the background of laser Doppler blood flowmeter. The proposed system implementation and design considerations are detailed in Section III. Measurement results of the LDF prototype are presented in section IV, with a conclusion made in section V.

II. Background on Laser Doppler Blood Flowmeter

The Doppler effect offers a unique property to quantify blood flow [15]. For the red blood cells (RBC) moving with a velocity v in the peripheral arteries, the well-known Doppler effect leads to a frequency shift between the incident light (e.g., a single wavelength in an ideal case) and the light scattered back by the RBCs. The resulted frequency shift depends on v, the incident LED light's wavelength λ, and the scattering angle θ, expressed as

$$f_{\text{shift}} = \frac{v}{\lambda} \cdot sin(\theta) \tag{1}$$

where f_{shift} reflects the changes in v. Meanwhile, the polarity of f_{shift} indicates the direction of blood flow, e.g., towards or away from the sensory system, as shown in Fig. 1(b). In practice, f_{shift} consists of multiple frequencies (i.e., a broadband [15]) as the RBC can move at different speed due to collision, etc., and a blood flowmeter typically measures the short-term averaged blood flow. Blood velocity measurements for various arteries were performed [16] and [17], where the reported signal bandwidth lies in a spectrum up to ~20 kHz. Typically, the blood flow rate in the artery with a diameter from 800 µm to 1.8 mm ranges between 2.3 ~ 26 mL/min [18], which is velocity-dependent defined as

$$Flow = \alpha \cdot \int_{\omega_1}^{\omega_2} \omega P(\omega) d\omega \tag{2}$$

where $\{\omega_i = 2\pi f_i,\ i = 1,2\}$, and the band of interest f_1, f_2 are usually designed to be 20 Hz and 20 kHz, respectively, to include the target signal but exclude the DC signal. $P(\omega)$ is the power spectrum (in A^2/Hz) of the photo current. The term α (unit: mL/min/A^2) is a constant to correlate the sensed photocurrent power to velocity. For laser Doppler-based blood flow measurement, the corresponding photocurrent change due to a small blood velocity change (e.g., cm/sec) is in the range of 10's to 100's of pA depending on the incident light power, skin conditions, and the blood flow speed. To measure such

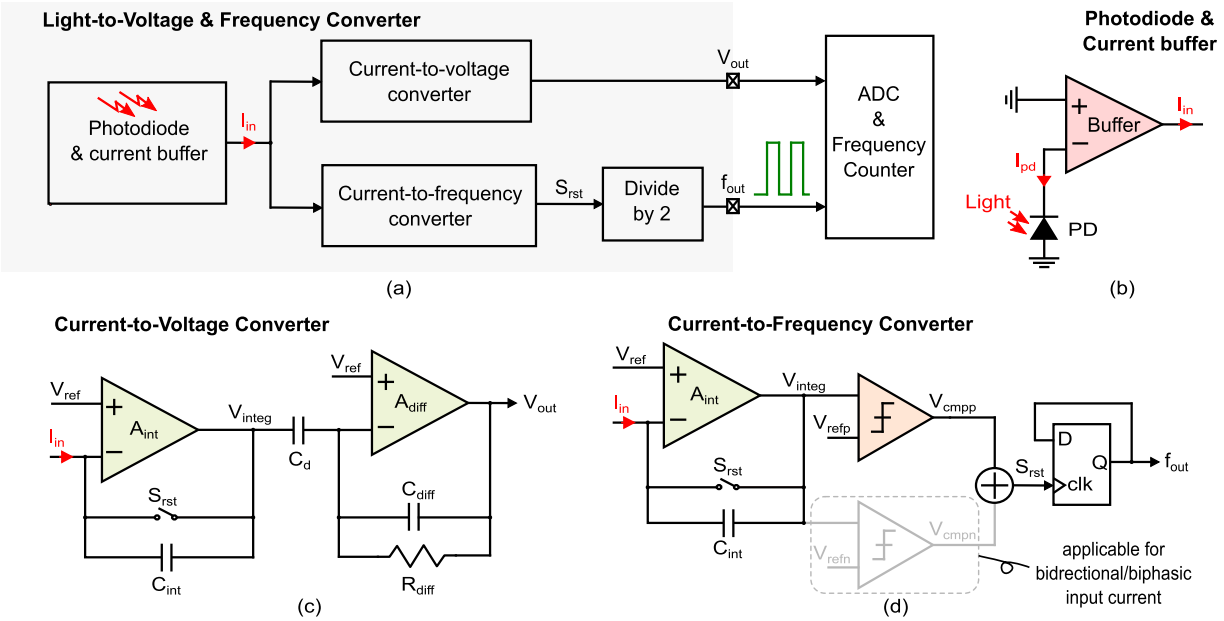

Fig. 2. Developed current measurement system; (a) the overall architecture including photocurrent to voltage and to frequency converters; (b) photodiode and current buffer; (c) integrator-differentiator transimpedance amplifier (TIA), and (d) current to frequency converter.

a tiny velocity variation, a sensitive photodiode (e.g., >80%) and high transimpedance gain (e.g., >20 MΩ [19]) is usually required.

As reported in [20], green, blue, and yellow light can reach the superficial capillary bed and the arterioles in the dermis as shown in Fig. 1(c). Whereas longer wavelengths such as red and infra-red can penetrate the skin and are able to reach the arteries between the dermis and subcutaneous tissue, and is employed in this work. During measurement, red light emitted from a LED with an integrated reflector (LS-T67F) having a wavelength of 630 ∼ 645 nm shines over the anterior or posterior tibial artery in the legs through the skin. The light scattered by the RBCs is collected by a photodiode (a peak sensitivity of >80% for 550 ∼ 650 nm wavelength using [22]). The reflected light experiences a Doppler shift induced by the RBC moving within the peripheral arteries at a certain velocity. In contrast, the light frequency reflected by the dormant RBCs and tissues stays unchanged. The sensing device measures the averaged frequency signal in a small band instead of a single modulated frequency, which is a low pass operation that rejects the sudden high-frequency and ambulatory artifacts. Meanwhile, for proof-of-concept, this work assumes a uniform tissue and light reflection angle.

III. System Implementation and Design Considerations

A. Overall System Description

Current measurement analog front-ends (AFE) have been extensively described and analyzed in the literature [23]. However, many designs have limited dynamic range primarily because of the circuit noise and supply voltage, limiting their minimum and maximum input currents, respectively. In addition, digital output is often desired for further signal processing, the front-end should be able to function as a low-noise signal amplifier, as well as an analog-to-digital converter [24]. Recently, system architectures based on light-to-frequency conversion have gained popularity due to their ability to combine integration, filtering, and digitization of the photocurrent in a compact manner [25], and is adopted in this work.

Fig. 2(a) shows the developed current measurement AFE. It consists of a photodiode, an input current buffer, a current-to-voltage converter, a current-to-frequency converter, and a modulo-two counter. This AFE is designed to provide both voltage and frequency output, V_{out} and f_{out}, respectively. Specifically, the voltage mode operation is preferred when the input current signal is small in magnitude and a high-precision ADC is present. On the other hand, the frequency mode performs better with large input currents from the photodiode. Therefore, This AFE can switch between the frequency and voltage modes of operation to maximize the measurable current range. By using a current buffer after the photodiode as in Fig. 2(b), the large parasitic capacitance of the photodiode does not directly load the integrator input [A_{int} in Fig. 2(c)(d)].

B. Readout Circuit Operation

The current-to-voltage converter shown in Fig. 2(c) employs an integrator-differentiator topology. Its voltage output is

$$V_{\text{out}} = V_{\text{ref}} + (R_{\text{diff}} \cdot I_{\text{in}}) \cdot \frac{C_{\text{d}}}{C_{\text{int}}} \tag{3}$$

where V_{ref} is a reference voltage designed to be $V_{\text{DD}}/2$, $C_{\text{int}} = 2$ pF is the integration capacitor, $R_{\text{diff}} = 4$ MΩ and $C_{\text{d}} = 20$ pF are the feedback resistance and capacitance of the differentiator, respectively. S_{rst} is an asynchronous control for the self-reset switch to limit the output of the integrator to be within a predefined voltage window set by V_{refP}. As shown in Fig. 2(d), when the integrator output V_{integ} crosses the

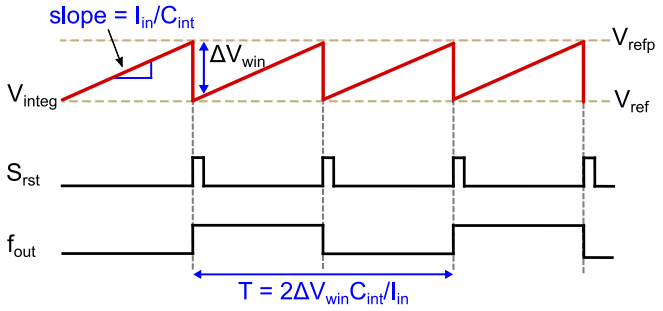

Fig. 3. Timing diagram of the integrator output V_{integ} with a positive current from the current buffer, the reset signal S_{rst}, and the frequency output f_{out}.

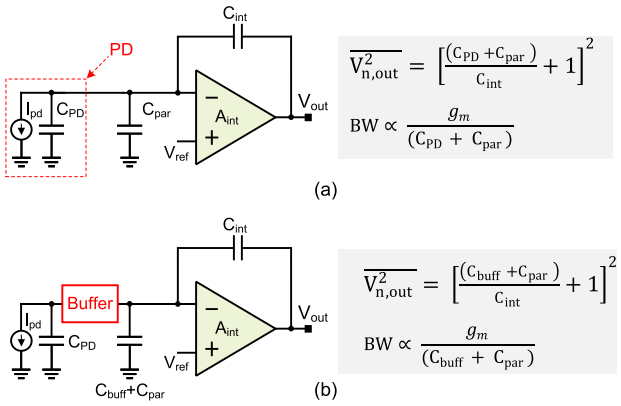

Fig. 4. Photodiode parasitic capacitance model and its influence on the integrator bandwidth: (a) without input current buffer, (b) with input current buffer.

predefined threshold voltage, the comparator is triggered and V_{integ} is compared with V_{refP} to produce S_{rst}. The output of the integrator is bounded by $\Delta V_{\text{win}} = V_{\text{refP}} - V_{\text{ref}}$ to avoid integrator linearity degradation. The selection of ΔV_{win} also affects the SNR of the frequency output as elaborated in section III-C.3.

This self-control scheme can produce a frequency output f_{out} almost for free with only one extra D flip-flop. To derive the relationship between f_{out} and I_{in}, Fig. 3 shows the timing diagram of the integrator output V_{integ}, S_{rst}, and f_{out} for a positive current I_{in} from the current buffer. When V_{integ} exceeds V_{refp}, S_{rst} triggers, thus resetting the integrator output to V_{ref}, which again resets S_{rst} (the pulse width of S_{rst} shown in Fig. 3 is exaggerated for illustration purpose). Therefore, the output frequency f_{out} can be expressed as

$$f_{\text{out}} = \frac{I_{\text{in}}}{2 \cdot \Delta V_{\text{win}} \cdot C_{\text{int}}} \tag{4}$$

where, I_{in} can be represented as

$$I_{\text{in}} = A \cdot sin(2\pi f_{\text{pd}} t) \tag{5}$$

where f_{pd} is the frequency (a broadband) of the incoming Doppler shifted light. Therefore, f_{out} is proportional to the buffered frequency modulated photocurrent, with

$$f_{\text{out}} = \frac{A \cdot sin(2\pi f_{\text{pd}} t)}{2 \cdot \Delta V_{\text{win}} \cdot C_{\text{int}}}. \tag{6}$$

As observed in Fig. 2(d), the proposed self-resetting current-to-frequency conversion topology does not require an external reset or clock signal. Thus the bandwidth of the system is not limited by a predefined sampling clock.

C. Circuit Design Consideration

1) Input Current Buffer: The first stage of the AFE is a current buffer following the photodiode. This design employs a current conveyor-based current buffer (AD844JRZ). It performs the decoupling and linear operations in current mode the same way as voltage buffer performs in voltage mode [23]. This second generation current conveyor (CC-II) architecture with a low input impedance input stage can minimize the input signal attenuation and it is insensitive to the stray capacitance when connected to the photodiode. This buffer also prevents the photodiode parasitic capacitor (40 pF to 135 pF for the selected model [22]) from loading the succeeding stage of the AFE.

Fig. 4 details the functionality and advantages of adopting a current buffer. The design parameters listed in the figure are the transconductance g_{m} of A_{int}, the input parasitic capacitance C_{par} of A_{int}, the photodiode parasitic capacitance C_{PD}, the current buffer output capacitance C_{buff}, and the integrator bandwidth BW. As in Fig. 4(a), if not isolated, C_{PD} would greatly increase the integrator output noise $\overline{V_{\text{n,out}}^2}$ (a few 10's of times). Even worse, as $C_{\text{PD}} \gg C_{\text{par}}$ (~3.5 pF for the adopted amplifier), it would mandate at least 10 times larger g_{m}, thus power consumption, of A_{int} in order for the integrator to achieve the same speed (BW) after interfacing with the photodiode. With an input current buffer, the junction capacitance from the photodiode can be isolated to avoid such a detrimental capacitive divider effect. As a result, adding a buffer to the system does not burn more power but saves power compared to connecting the photodiode directly to an integrator.

2) Current-to-Voltage Converter: The C-V converter in our design employs a continuous-time integrator-differentiator architecture as shown in Fig. 2(c) [26]–[28], which is known for small input current measurements. The high gain of the integrator stage ensures low noise density, whereas the differentiator stage yields a flat frequency response [29]. It is usually designed with $C_{\text{d}}/C_{\text{int}} \gg 1$ and a large differentiator resistor R_{diff} to make the thermal noise of R_{diff} negligible, thus minimizing the equivalent input noise. However, different from the conventional designs, our system is limited by the bandwidth requirements, i.e., 20 kHz, therefore, R_{diff} will be chosen such that it can fulfill the bandwidth requirement. The equivalent input-referred current noise density of this converter is [30]

$$\overline{I_{\text{n,in}}^2} = \overline{V}_{\text{n,Aint}}^2 \cdot [(2\pi f)^2 (C_{\text{int}} + C_{\text{par}})^2] + \frac{4kT}{R_{\text{diff}}} \cdot \left(\frac{C_{\text{int}}}{C_{\text{d}}}\right)^2 \tag{7}$$

where k is the Boltzmann constant, T is the absolute temperature, and $\overline{V}_{\text{n,Aint}}^2 \approx 8\ \text{nV}/\sqrt{Hz}$ is the input noise density of the adopted amplifier A_{int} (LTC6244 [31]). It can be

found that although the thermal noise of R_{diff} is scaled by $(C_{\text{int}}/C_{\text{d}})^2$ when referring to the input. As $R_{\text{diff}} = 4$ MΩ is not large enough, it will be the dominant noise source of the designed integrator-differentiator TIA.

Besides noise and dynamic range considerations, the frequency response of the converter should also be considered. We assume A_{diff} has a dominant pole f_0 and a DC gain of A_{d}. The −3 dB frequency and the damping factor ξ of the system [Fig. 2(c)] is given by [19] and [29]

$$f_{\text{H}} = \frac{1}{2\pi \cdot R_{\text{diff}} \cdot C_{\text{diff}}} \tag{8}$$

$$\xi = \sqrt{\frac{R_{\text{diff}} C_{\text{diff}}^2 \cdot A_{\text{d}} f_0}{4(C_{\text{diff}} + C_{\text{d}})}}. \tag{9}$$

To minimize the overshoot and ringing in the signal mid-band, (10) should hold

$$GBW = A_{\text{d}} f_0 \geqslant \frac{(C_{\text{diff}} + C_{\text{d}})}{C_{\text{diff}}} \cdot \frac{4\xi^2}{2\pi \cdot R_{\text{diff}} \cdot C_{\text{diff}}} \tag{10}$$

where $\xi \geqslant 1/\sqrt{2}$ is often required. With $C_{\text{diff}} = 2$ pF, $C_{\text{d}} = 20$ pF and $R_{\text{diff}} = 4$ MΩ, a transimpedance gain of 40 MΩ and a –3 dB bandwidth of 20 kHz can be achieved to meet our target application requirements.

3) Current-to-Frequency Conversion: For the C-F conversion, outputs from the comparator is firstly XOR-ed, followed by a D-Flip flop in its modulo-2 configuration to produce f_{out}. This asynchronously generated frequency output does not contain quantization noise [32]. Despite that, several other factors can still contribute noise and nonlinearities. The voltage noise of the comparator is one of the critical factors, as it introduces clock jitter. Once V_{integ} crosses V_{refP} (and V_{refN} for biphasic input), the input-referred voltage noise of the comparator will introduce a stochastic delay to the rising and falling edge of the frequency output. Referring to the datasheets of the adopted devices, the calculated total voltage noise at the input of the comparator is $\overline{V_{\text{n}}^2} \approx 107.74$ fV^2/Hz, which is composed of the output referred noise of the integrator $\overline{V^2}_{\text{n,integ}}$ and the input-referred noise of the comparator (LTC1441 [33]) $\overline{V^2}_{\text{n,cmp}}$. After the comparison operation, the clock jitter at the output of the comparator can be quantified as [34]

$$\delta_{\text{jitter-fout}} = \overline{V}_{\text{n,inband}} \cdot \frac{C_{\text{int}}}{I_{\text{in}}} \tag{11}$$

where $\overline{V}_{\text{n,inband}}$ is the total in-band noise at the input of the comparator. The clock jitter limits the minimum detectable change in f_{out}, which in turn limits the minimum detectable input current change from the photodiode. Note that the frequency output period is $T_{\text{out}} = 2\Delta V_{\text{win}} \cdot C_{\text{int}}/I_{\text{in}}$ as derived from (4). So the signal-to-noise ratio of the frequency readout $\text{SNR}_{\text{fout}} \approx T_{\text{out}}/\sigma_{\text{jitter-fout}} \approx \Delta V_{\text{win}}/\overline{V}_{\text{n,inband}}$. A larger ΔV_{win} or by reducing the total voltage noise referred to the comparator input node can improve the SNR of the frequency output. Thus, with $\overline{V}_{\text{n,inband}} \approx 47$ μVrms in 20 kHz bandwidth, and $\Delta V_{\text{win}} = 800$ mV, the frequency readout SNR is approximately 80 dB.

The nonlinearity in f_{out} is primarily caused by charge injection from the reset switches in the integrator feedback path and propagation delay in the digital control logic. Whenever S_{rst} toggles, it introduces an error voltage at the start of the next conversion cycle due to switch charge injection. The delay in the reset operation is due to the delay of the XOR gate, DFF, and comparator, which can be addressed by using high-speed components. Experimental results show that for large input currents, the corresponding nonlinearity increases.

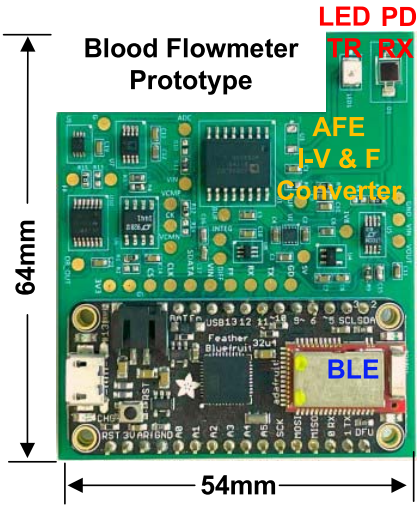

Fig. 5. Designed proof-of-concept board of the blood flowmetry system.

IV. Device Prototype and Measurement

A. Prototype

In this work, discrete components were used to build a proof-of-concept prototype as shown in Fig. 5(a). Since a low-cost fully-integrated laser was not available, we implemented the excitation light with a narrow band LED to fulfill the requirements. The transmitter comprising a constant current linear LED driver (AL5809), and the LED itself. The LED has a peak wavelength sensitivity at 630 nm. The receiver embodies a photodiode, which is sensitive to a wavelength range of 627 nm ∼ 645 nm, followed by the AFE comprising both the current to voltage and to frequency converters.

A 3.3-V LDO provides a stable supply. A reference voltage generator is also implemented to provide the required bias for the integrator, differentiator, and comparators. The differentiator is implemented as a band-pass filter, and it sets the high cut-off frequency f_{H} of the whole readout. Note that f_{H} can be handily adjusted for different types of applications and patients based on their age and medical history (e.g., patients suffering with heart disease or taking certain medicines) by simply tuning C_{diff} without compromising the in-band gain or noise performance of the AFE. The opamp chosen for the integrator has an input capacitance of only a few pF. Furthermore, a MOS-input base opamp LTC6244 with a low input bias current of 1 pA is employed. Fig. 6 shows the power consumption distribution of different modules of this prototype (108.9 mW in total). The current buffer in our design is the most power-hungry block as it must be low-noise and it requires an additional boost converter to meet its power supply requirements (i.e., 5-V).

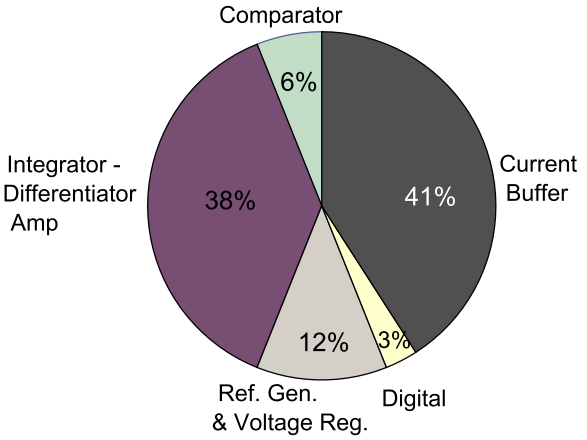

Fig. 6. Power consumption distribution of different building blocks of the prototype.

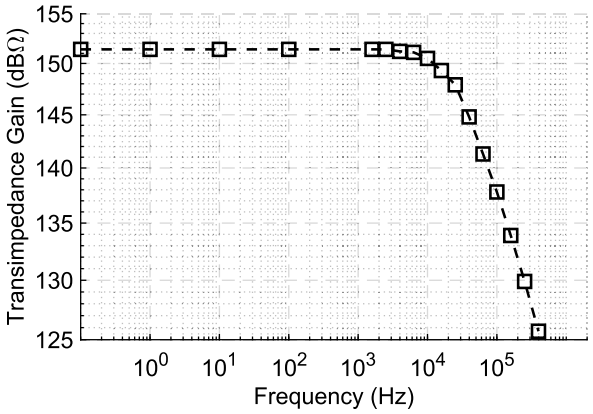

Fig. 7. Frequency response and transimpedance gain (V_{out}/I_{in}) of the integrator-differentiator based TIA.

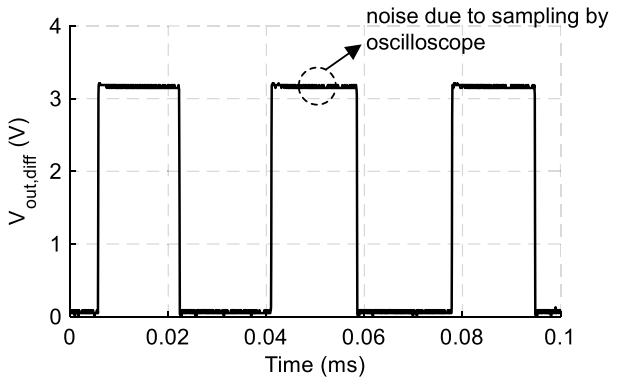

Fig. 8. Measurement results of the differentiator output V_{out} with an 80 nA input current (on-off modulated) to the current buffer.

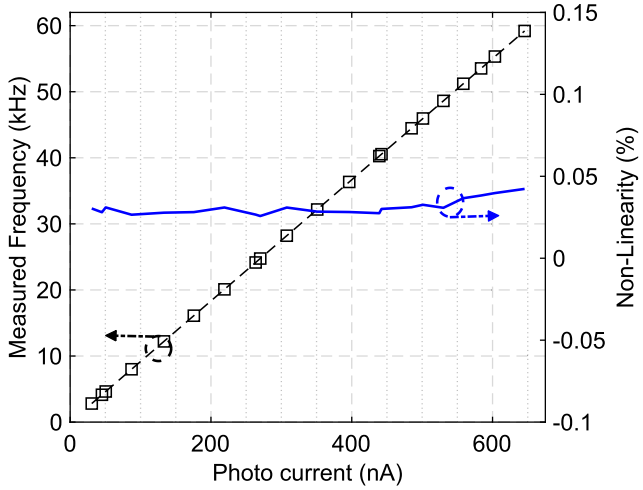

Fig. 9. Measured frequency output and nonlinearity of f_{out} with respect to I_{PD} (modulated to 5 kHz).

B. Measurement

The fabricated system is characterized by two individual set-ups. First, in the electrical testing, the input current is varied to measure the corresponding frequency and voltage outputs. The second experiment involved a demo biological set-up. A fluid having silicon micro-spheres to imitate RBCs in the blood was pumped to maintain a particular flow rate and the corresponding output frequency was recorded.

1) Electrical Measurement: Based on the calculations and simulations, the integrator-differentiator-based current-to-voltage converter is designed with a transimpedance gain of 152 dBΩ and a −3dB bandwidth of 20 kHz. In contrast, the measured transimpedance gain is 151.4 dBΩ with a −3 dB bandwidth of approximately 18.9 kHz due to device imperfections and parasitics in routing, etc. The measured frequency response of the integrator-differentiator TIA is shown in Fig. 7. The measured minimum detectable input current is 41.7 pA (measured in a full dark condition). Fig. 8 presents the differentiator output V_{out} for a modulated 80 nA input current to the current buffer, which is the maximum input current that can be handled by the voltage mode of the readout to avoid TIA saturation. The voltage mode output can be quantized by the 10-bit ADC from the ATmega32U4 controller we employed (see Fig. 5). For inputs larger than 80 nA, the frequency mode of the converter could be used to boost the overall input dynamic range when it is required to measure a large flow. The current-to-frequency converter is characterized under different I_{PD} (modulated to 5 kHz). The measurement results in Fig. 9 shows f_{out} and its nonlinearity. The maximum recorded frequency output is for $I_{PD} \approx 650$ nA to maintain a 0.05% system linearity. As a result, the input range of our designed converter is from 41.7 pA to 650 nA, operating in different modes depending on the actual input current amplitude. In the following microfluid testing, we will use the frequency mode to demonstrate the device performance with imitated blood flow.

2) Biomemitic Microfluid Measurement: To demonstrate the blood flow measurement using our system, we recorded f_{out} by changing an imitated blood flow through a syringe pump. The overall measurement setup is shown in Fig. 10(a). We used a syringe pump in conjunction with syringes and tubing that can hold volumes between 1 mL and 5 mL to control the fluid flow. The flow and circulation were arranged to avoid air bubbles. Moreover, to minimize turbulent or unsteady flow, the tubing and syringe were kept straight at a distance of at least five times the diameter of the tube. Bio-mimetic silica

TABLE I
PERFORMANCE COMPARISON WITH OTHER CURRENT SENSING FRONT-END FOR BIOMEDICAL APPLICATIONS

	CMOS integrated				Discrete implementation		
Reference	[23]	[28]	[37]	[36]	[19]	[35]	**This Work**
Application	Nanoparticles, nanopores	Single molecule sensing	Near infrared spectroscopy	Bilayer lipid membrane	DNA sequencing	Biomolecules	**Blood flowmetery**
Technology	0.5 µm CMOS	0.35 µm CMOS	0.18 µm CMOS	0.35 µm CMOS	Discrete IC	Discrete IC	**Discrete IC**
Supply	3.3 V	1.5 V	3.3 V	3.3 V	±5 V	±10 V	**3.3 V**
Signal bandwidth	50 Hz to 50 kHz	4 MHz	20 Hz	10 kHz	950 kHz	1.4 MHz	**18.9 kHz**
Max input current	13 nA	25 nA	200 µA	20 nA	158 nA	10 nA	**650 nA**
Dynamic range	74 dB	95.9 dB	95 dB	/	93.3 dB	/	**83.9 dB**
Sampling clock	100 Hz to 100 kHz	not required	2 kHz	20 kHz	not required	not required	**not required**
Transimpedance gain	/	146 dBΩ	130 dBΩ	/	149 dBΩ	146 dBΩ	**151.4 dBΩ**
System power	1.5 mW	45 mW†	0.196 mW	40 mW	65 mW†	650 mW†	**108.9 mW**

†Power consumption of integrator-differentiator based TIA only

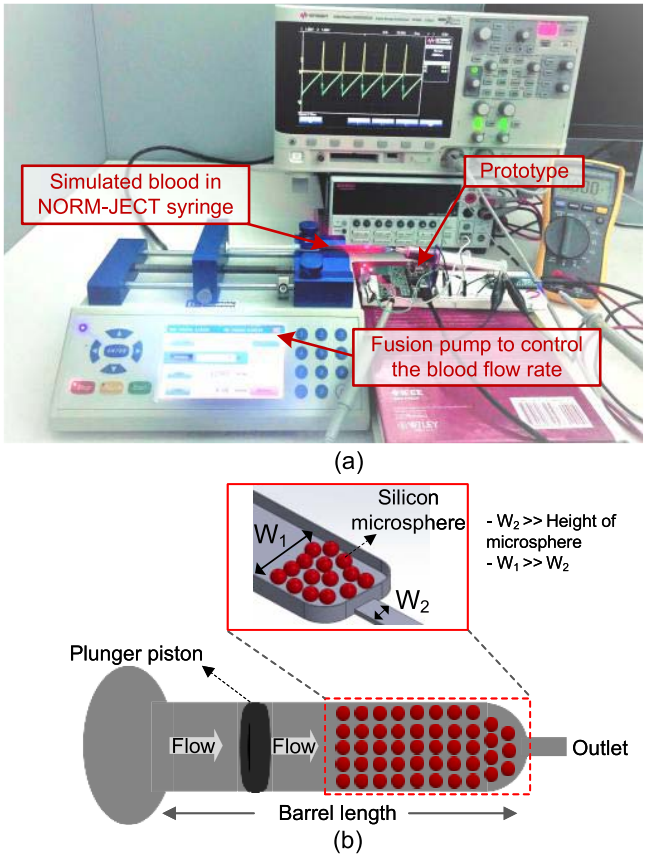

Fig. 10. (a) Microfluidic measurement setup; (b) simulated blood using bio-mimetic micro spheres mixed with saline water.

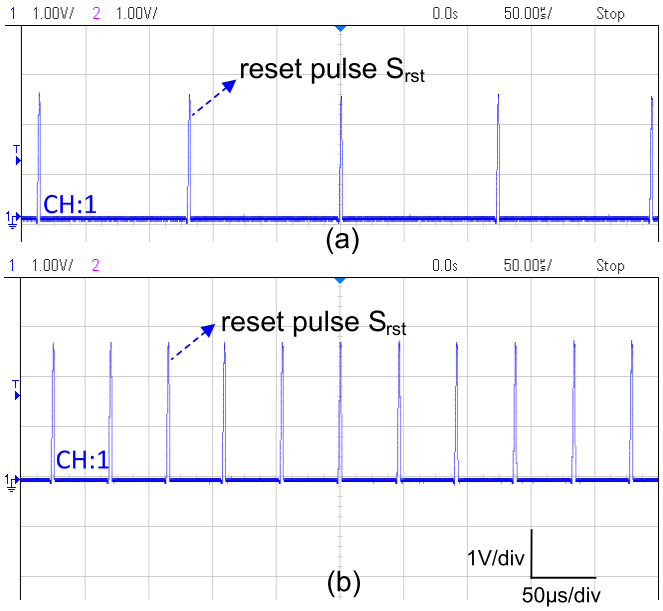

Fig. 11. Measurement results of microfluid (imitated blood) testing; (a) S_{rst} at a programmed flow rate of 0 mL/min (stationary); (b) S_{rst} at a programmed flow rate of 4.3 mL/min.

microspheres are commonly used for biological measurement, as they exhibit uniform ordering and pore sizing, while providing a high surface area to volume ratio. In this experiment, silicon micro spheres are mixed with saline water to mimic the RBCs. Their pore properties offer an excellent way to deliver and store inter-cellular materials, exhibiting RBC-like environment. Considering the high binding capability of microbeads, we diluted 2 mg (absolute number $0.70\sim1.50 \times 10^8$) of silica microbeads in 1 mL of saline water, which is similar to the amount of RBCs in human blood.

The fusion pump was calibrated and programmed between 0 and 4.3 mL/min. The output frequency was firstly recorded when the fluid was stationary to develop the baseline measurement, as shown in Fig.11(a). The non-zero frequency output is mainly due to the DC signal from the photodiode, which is not suppressed in the readout. Afterwards, the output at a flow of 4.3 mL/min was recorded as in Fig.11(b). To characterize the system linearity, the flow rate was varied step-wise from 0.1 mL/min to 4.3 mL/min. The recorded frequency output corresponding to the programmed blood flow range and their associated nonlinearities are shown in Fig. 12. The measurement results show <1% nonlinearity between the flow rate and the corresponding output frequency in this simulated testing.

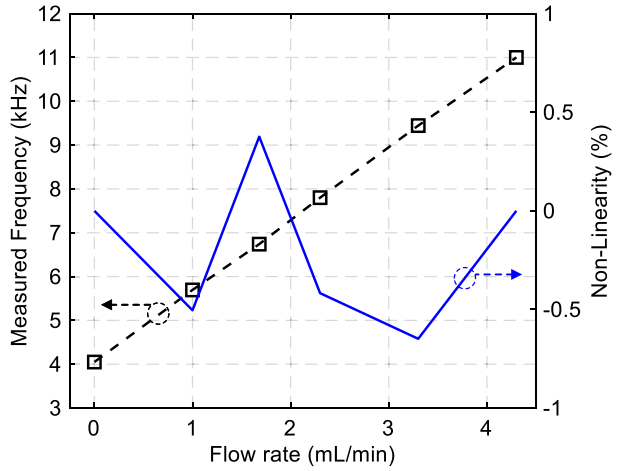

Fig. 12. Measured output frequency versus flow rate and the corresponding nonlinearity (end-point method).

Table I summarizes the performance of our proof-of-concept device and compares our work with prior arts. With our proposed asynchronous architecture where the predefined sampling clock does not limit the maximum input, this work achieves a large maximum measurable current of 650 nA with 0.05% readout linearity. Meanwhile, the integrator-differentiator TIA designs in [19], [27], [28], and [36] as well as the current-to-frequency converters in [24] and [37], employ a DC-servo loop and a mixed-signal feedback loop, respectively, to prevent the output of the integrator from saturation, which inevitably increases their design complexity as well as power consumption. In contrast, our design does not require such a loop, as the asynchronous self-resetting mechanism will prevent the output of the integrator from saturation by limiting the output of the integrator to be within a predefined voltage window.

V. Conclusion

A blood flow measurement prototype has been presented for patients suffering from PAD disease. By combining the photocurrent sensing mechanism with Doppler effect, we have successfully measured the blood flow variations in constricted tubes that emulate human peripheral arteries. Our system can evaluate the flow states and provide quantitative data essential in making early decisions. Our proposed system features both the optical and electrical modules integrated on a single PCB with a dimension of 55 mm $\times$ 65 mm and does not require optical fiber or filter. Consequently, by avoiding the dynamic artifacts, improved noise performance and reduced coupling loss have been achieved. Because of its compact size (will be further scaled down), this integrated blood flowmeter can be applied in home-care settings as a self-monitoring wearable health system.

References

[1] N. Ushiroyama, "Clinical analysis and correspondence with pathological condition of chills-what pathological condition is observed by the chills? Can it be cured?" *J. Clin. Exp. Med.*, vol. 215, no. 11, pp. 925–929, 2005.

[2] K. Kuwabara, Y. Higuchi, H. Koizumi, and R. Kasahara, "Blood flow observed with smartphone-ultracompact wearable blood flow sensor," *NTT Tech. Rev.*, vol. 13, no. 1, pp. 1–6, Jan. 2015.

[3] H. Akahori *et al.*, "Impact of peripheral artery disease on prognosis after myocardial infarction: The J-MINUET study," *J. Cardiol.*, vol. 76, no. 4, pp. 402–406, Oct. 2020.

[4] T. Kiyokura, S. Mino, and J. Shimada, "Wearable laser blood flowmeter," *NTT Tech. Rev.*, vol. 4, no. 1, pp. 38–43, 2006.

[5] M. R. Babaei, M. Malek, F. T. Rostami, Z. Emami, N. H. Madani, and M. E. Khamseh, "Non-invasive vascular assessment in people with type 2 diabetes: Diagnostic performance of plethysmographic-and-Doppler derived ankle brachial index, toe brachial index, and pulse volume wave analysis for detection of peripheral arterial disease," *Primary Care Diabetes*, vol. 14, no. 3, pp. 282–289, Jun. 2020.

[6] G. Mahé, G. Leftheriotis, J. Picquet, V. Jaquinandi, J. L. Saumet, and P. Abraham, "A normal penile pressure cannot rule out the presence of lesions on the arteries supplying the hypogastric circulation in patients with arterial claudication," *Vascular Med.*, vol. 14, no. 4, pp. 331–338, Nov. 2009.

[7] A. Ruiz-Vargas, S. A. Morris, R. H. Hartley, and J. W. Arkwright, "Optical flow sensor for continuous invasive measurement of blood flow velocity," *J. Biophoton.*, vol. 12, no. 10, Oct. 2019.

[8] W. Iwasaki, H. Nogami, S. Takeuchi, M. Furue, E. Higurashi, and R. Sawada, "Detection of site-specific blood flow variation in humans during running by a wearable laser Doppler flowmeter," *Sensors*, vol. 15, no. 10, pp. 25507–25519, Oct. 2015.

[9] Q. Lin *et al.*, "Wearable multiple modality bio-signal recording and processing on chip: A review," *IEEE Sensors J.*, vol. 21, no. 2, pp. 1108–1123, Jan. 2021.

[10] B. Lin, Z. Ma, M. Atef, L. Ying, and G. Wang, "Low-power high-sensitivity photoplethysmography sensor for wearable health monitoring system," *IEEE Sensors J.*, vol. 21, no. 14, pp. 16141–16151, Jul. 2021.

[11] A. Atef, M. Atef, E. E. M. Khaled, and M. Abbas, "CMOS transimpedance amplifiers for biomedical applications: A comparative study," *IEEE Circuits Syst. Mag.*, vol. 20, no. 1, pp. 12–31, 1st Quart., 2020.

[12] M. Draijer *et al.*, "Twente optical perfusion camera: System overview and performance for video rate laser Doppler perfusion imaging," *Opt. Exp.*, vol. 17, no. 5, pp. 3211–3225, 2009.

[13] Moor Instruments. *Laser Doppler Monitor*. Accessed: Oct. 2020. [Online]. Available: https://www.moor.co.U.K./products/monitoring/high-power-laser-doppler-monitor

[14] D. Watkins and G. A. Holloway, "An instrument to measure cutaneous blood flow using the Doppler shift of laser light," *IEEE Trans. Biomed. Eng.*, vol. BME-25, no. 1, pp. 28–33, Jan. 1978.

[15] M. A. Quiñones, C. M. Otto, M. Stoddard, A. Waggoner, and W. A. Zoghbi, "Recommendations for quantification of Doppler echocardiography: A report from the Doppler quantification task force of the nomenclature and standards committee of the American society of echocardiography," *J. Amer. Soc. Echocardiogr.*, vol. 15, no. 2, pp. 167–184, Feb. 2002.

[16] D. He *et al.*, "Laser Doppler blood flow imaging using a CMOS imaging sensor with on-chip signal processing," *Sensors*, vol. 13, no. 9, pp. 12632–12647, Sep. 2013.

[17] R. Charles *et al.*, "Laser Doppler measurements of blood flow in capillary tubes and retinal arteries," *Investigative Ophthalmol. Vis. Sci.*, vol. 11, no. 11, pp. 936–944, Nov. 1972.

[18] M. Klarhöfer, B. Csapo, C. Balassy, J. C. Szeles, and E. Moser, "High-resolution blood flow velocity measurements in the human finger," *Magn. Reson. Med.*, vol. 45, no. 4, pp. 716–719, May 2001.

[19] C.-L. Hsu, H. Jiang, A. G. Venkatesh, and D. A. Hall, "A hybrid semi-digital transimpedance amplifier with noise cancellation technique for nanopore-based DNA sequencing," *IEEE Trans. Biomed. Circuits Syst.*, vol. 9, no. 5, pp. 652–661, Oct. 2015.

[20] J. Liu, B. P.-Y. Yan, W.-X. Dai, X.-R. Ding, Y.-T. Zhang, and N. Zhao, "Multi-wavelength photoplethysmography method for skin arterial pulse extraction," *Biomed. Opt. Exp.*, vol. 7, no. 10, pp. 4313–4326, Sep. 2016.

[21] E. Sorbellini, M. Rucco, and F. Rinaldi, "Photodynamic and photobiological effects of light-emitting diode (LED) therapy in dermatological disease: An update," *Lasers Med. Sci.*, vol. 33, no. 7, pp. 1431–1439, Sep. 2018.

[22] OSRAM Opto Semiconductors. *SFH 2440*. Accessed: Oct. 2020. [Online]. Available: https://tz.micro-semiconductor.hk/datasheet/57-SFH-2440.pdf

[23] B. Goldstein, D. Kim, J. Xu, T. K. Vanderlick, and E. Culurciello, "CMOS low current measurement system for biomedical applications," *IEEE Trans. Biomed. Circuits Syst.*, vol. 6, no. 2, pp. 111–119, Apr. 2012.

[24] F. Marefat, R. Erfani, and P. Mohseni, "A 1-V 8.1-μW PPG-recording front-end with >92-dB DR using light-to-digital conversion with signal-aware DC subtraction and ambient light removal," *IEEE J. Solid-State Circuits Lett.*, vol. 3, pp. 17–20, 2020.
[25] A. Hedayatipour, S. Aslanzadeh, S. H. Hesari, M. A. Haque, and N. McFarlane, "A wearable CMOS impedance to frequency sensing system for non-invasive impedance measurements," *IEEE Trans. Biomed. Circuits Syst.*, vol. 14, no. 5, pp. 1108–1121, Oct. 2020.
[26] M. Ahmed, M. A. Awan, M. A. Atta, and A. Bermak, "Ambient light suppression in visible light transceivers: A review," in *Proc. 4th Int. Conf. Circuits, Syst. Simulation (ICCSS)*, May 2021, pp. 207–211.
[27] G. Ferrari, F. Gozzini, and M. Sampietro, "A current-sensitive front-end amplifier for nano-biosensors with a 2 MHz BW," in *IEEE Int. Solid-State Circuits Conf. (ISSCC) Dig. Tech. Papers*, Feb. 2007, pp. 164–165.
[28] G. Ferrari, F. Gozzini, A. Molari, and M. Sampietro, "Transimpedance amplifier for high sensitivity current measurements on nanodevices," *IEEE J. Solid-State Circuits*, vol. 44, no. 5, pp. 1609–1616, May 2009.
[29] S. Dai, R. T. Perera, Z. Yang, and J. K. Rosenstein, "A 155-dB dynamic range current measurement front end for electrochemical biosensing," *IEEE Trans. Biomed. Circuits Syst.*, vol. 10, no. 5, pp. 935–944, Oct. 2016.
[30] M. A. Awan, B. Wang, N. A. Quadir, and A. Bermak, "Review and analysis of CMOS current readout circuits for biosensing applications," in *Proc. IEEE Int. Symp. Circuits Syst. (ISCAS)*, May 2021, pp. 1–5.
[31] Analog Devices. *Low Noise CMOS Opamp*. Accessed: Oct. 2020. [Online]. Available: https://www.mouser.com/datasheet/2/609/6244fb-1267547.pdf
[32] S. Ouzounov, E. Roza, J. A. Hegt, G. van der Weide, and A. H. M. van Roermund, "Analysis and design of high-performance asynchronous sigma-delta modulators with a binary quantizer," *IEEE J. Solid-State Circuits*, vol. 41, no. 3, pp. 588–596, Mar. 2006.
[33] Linear Technology. *Ultralow Power Single/Dual Comparator With Reference*. Accessed: Oct. 2020. [Online]. Available: https://www.mouser.com/datasheet/2/609/144012fd-1269570.pdf
[34] Q. Lin *et al.*, "A 119 dB dynamic range charge counting light-to-digital converter for wearable PPG/NIRS monitoring applications," *IEEE Trans. Biomed. Circuits Syst.*, vol. 14, no. 4, pp. 800–810, Aug. 2020.
[35] G. Ferrari and M. Sampietro, "Wide bandwidth transimpedance amplifier for extremely high sensitivity continuous measurements," *Rev. Sci. Instrum.*, vol. 78, no. 9, Sep. 2007, Art. no. 094703.
[36] M. Crescentini *et al.*, "A distributed amplifier system for bilayer lipid membrane (BLM) arrays with noise and individual offset cancellation," *IEEE Trans. Biomed. Circuits Syst.*, vol. 9, no. 3, pp. 334–344, Jun. 2015.
[37] Q. Lin *et al.*, "A 28 μW 134 dB DR 2nd-order noise-shaping slope light-to-digital converter for chest PPG monitoring," in *IEEE Int. Solid-State Circuits Conf. (ISSCC) Dig. Tech. Papers*, Feb. 2021, pp. 390–392.

Muhammad Asfandyar Awan (Graduate Student Member, IEEE) received the B.Eng. degree in electronics engineering from COMSATS University Islamabad, Pakistan, in 2009, and the M.Eng. degree in electrical and electronics engineering from Linköping University, Sweden, in 2012. He is currently pursuing the Ph.D. degree with the Division of Information and Computing Technology, College of Science and Engineering, Hamad Bin Khalifa University (HBKU), Qatar.

From 2013 to 2017, he worked as a Research Assistant with the Microelectronics Circuits Center Ireland (MCCI) on low power, low-speed bio-medical front-end design. His research interests include analog mixed-signal circuit design, sensor interface, and current readouts for bio-medical applications.

Moaaz Ahmed (Member, IEEE) received the B.S. degree in electrical engineering from the University of Engineering and Technology, Peshawar, Pakistan, in 2007, and the Double-Badged Ph.D. degree in electronic and computer engineering from the Hong Kong University of Science and Technology, Hong Kong, and University of Western Australia, Australia, in 2017.

He is currently a Postdoctoral Fellow with the College of Science and Engineering, Hamad Bin Khalifa University, Qatar. His research interests include mixed-signal integrated circuit design, CMOS interfaces for MEMS sensors, image sensors, analog-to-digital converters, and visible light communication.

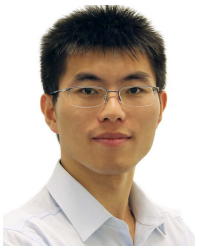

Bo Wang (Member, IEEE) received the B.Eng. (Hons.) degree in electrical engineering from Zhejiang University, Hangzhou, China, in 2010, and the M.Phil. and Ph.D. degrees in electronic and computer engineering from The Hong Kong University of Science and Technology (HKUST), Hong Kong, in 2012 and 2015, respectively.

In 2015, he joined HKUST as a Postdoctoral Researcher and led the HKUST-MIT Consortium Project on wireless sensing node design for smart green building applications. Afterwards, he was with the Massachusetts Institute of Technology in 2016, on low power data converter design for this project. In 2017, he joined Hamad Bin Khalifa University, Qatar, as a Founding Faculty, where he is currently an Assistant Professor with the Division of Information and Computing Technology, College of Science and Engineering. His research interests include energy-efficient analog mixed-signal circuits, sensor and sensor interface, and heterogeneous integrated systems for *in vitro/vivo* health monitoring.

Dr. Wang was a recipient of the IEEE ASP-DAC Best Design Award in 2016. He serves as a Technical Committee Member for the IEEE CAS Committee on Sensory Systems.